



## Orientation-dependent transport properties of Cu<sub>3</sub>Sn

Matthias Daeumer<sup>a,1</sup>, Ernesto D. Sandoval<sup>b,1</sup>, Arad Azizi<sup>a</sup>, Morteza H. Bagheri<sup>a</sup>,  
In-Tae Bae<sup>b,c</sup>, Sitaram Panta<sup>b</sup>, Ekaterina A. Koulakova<sup>b</sup>, Eric Cotts<sup>b</sup>, Charles L. Arvin<sup>d</sup>,  
Aleksy N. Kolmogorov<sup>b,\*</sup>, Scott N. Schiffrs<sup>a,\*</sup>

<sup>a</sup> Department of Mechanical Engineering, Binghamton University, 4400 Vestal Pkwy E, Binghamton, NY 13902, United States

<sup>b</sup> Department of Physics, Binghamton University, 4400 Vestal Pkwy E, Binghamton, NY 13902, United States

<sup>c</sup> Small Scale Systems Integration and Packaging Center, Binghamton University, 4400 Vestal Pkwy E, Binghamton, NY 13902, United States

<sup>d</sup> IBM, 2070 Route 52; Hopewell Junction, NY 12533, United States



### ARTICLE INFO

#### Article history:

Received 5 March 2021

Revised 17 December 2021

Accepted 16 January 2022

Available online 17 January 2022

### ABSTRACT

Cu<sub>3</sub>Sn, a well-known intermetallic compound with a high melting temperature and thermal stability, has found numerous applications in microelectronics, 3D printing, and catalysis. However, the relationship between the material's thermal conductivity anisotropy and its complex anti-phase boundary superstructure is not well understood. Here, frequency domain thermoreflectance was used to map the thermal conductivity variation across the surface of arc-melted polycrystalline Cu<sub>3</sub>Sn. Complementary electron backscatter diffraction and transmission electron microscopy revealed the thermal conductivity in the principal *a*, *b*, and *c* orientations to be 57.6, 58.9, and 67.2 W/m-K, respectively. Density functional theory calculations for several Cu<sub>3</sub>Sn superstructures helped examine thermodynamic stability factors and evaluate the direction-resolved electron transport properties in the relaxation time approximation. The analysis of computed temperature- and composition-dependent free energies suggests metastability of the known long-period Cu<sub>3</sub>Sn superstructures while the transport calculations indicate a small directional variation in the thermal conductivity. The ~15% anisotropy measured and computed in this study is well below previously reported experimental values for samples grown by liquid-phase electroepitaxy.

© 2022 Acta Materialia Inc. Published by Elsevier Ltd. All rights reserved.

### 1. Introduction

Technological and environmental factors have been driving the development of high-performance Pb-free integrated circuits with ultra-fine pitches and vertical integration [1,2]. The new microelectronic architectures have interconnects with dramatically reduced dimensions (20 μm) and require bonding materials capable of operating in high power density environments. Between-chip joints based on Cu-Sn compounds have shown several advantages over the conventional Sn-rich solders characterized by relatively low melting temperatures and susceptibility to liquid bridging. In particular, Cu-Sn-Cu couples that transform into Cu/Cu<sub>3</sub>Sn/Cu fully intermetallic joints benefit from the Cu<sub>3</sub>Sn alloy's high melting temperature (640 °C) [3], low electrical resistivity (8.8 μΩ-cm) [4], high resistance to electromigration and oxidation [5–8], and rapid bond formation (below 10 s at 250 °C with ultrasonic assistance) [9].

Despite the extensive research on Cu<sub>3</sub>Sn and the material's technological promise, the anisotropy of the thermal conductivity in this hexagonal close-packed (HCP)-based compound known to crystallize in different long-period superstructures [10–14] has not been studied. The only available information on the transport anisotropy<sup>2</sup> in Cu<sub>3</sub>Sn is the orientation-dependent measurement of the electrical conductivity in liquid-phase electroepitaxial samples by Liu et al. [10]. The maximum to minimum ratio of 2.8 found in that study might not seem extraordinarily large considering that the reported out-of-plane to in-plane conductivity ratios in pure HCP metals [15–19] range from 0.54 in Co (computed electrical transport  $\sigma_{zz}/\sigma_{xx}$ )<sup>3</sup> [15] to 2.9–5.4 in Fe at high pressure (measured thermal transport  $\kappa_{zz}/\kappa_{xx}$ ) [19]. However, the factor of 2.8 anisotropy in the thermal conductivity of a bonding material can have a drastic impact on the interconnect performance and dura-

\* Corresponding authors.

E-mail addresses: [kolmogorov@binghamton.edu](mailto:kolmogorov@binghamton.edu) (A.N. Kolmogorov), [sschiffr@binghamton.edu](mailto:sschiffr@binghamton.edu) (S.N. Schiffrs).

<sup>1</sup> These authors contributed equally to this work.

<sup>2</sup> The Wiedmann-Franz law discussed below is commonly used to relate thermal and electrical transport anisotropies. Our density functional theory results support the validity of the approximation for Cu<sub>3</sub>Sn.

<sup>3</sup> Sanborn et al. reported the Co anisotropy as the resistivity ratio  $\rho_{zz}/\rho_{xx} = 1.84$ . Here, we use the inverse to specify the conductivity ratio  $\sigma_{zz}/\sigma_{xx} = (\rho_{zz}/\rho_{xx})^{-1} = 0.54$ .

bility. For example, a hypothetical package with a 20  $\mu\text{m}$  thick  $\text{Cu}_3\text{Sn}$  film passing 10  $\text{W}/\text{mm}^2$  heat flux [20–24] would have temperature differences of 13  $^\circ\text{C}$  versus 4.5  $^\circ\text{C}$  in the slow versus fast directions. These temperature differences are significant given that the total thermal budget might be only 60–80  $^\circ\text{C}$  and that every  $\sim 7$   $^\circ\text{C}$  increase halves the mean time to electronic device failure [25].

The present investigation is focused on providing a better understanding of the anisotropic thermal conductivity of pure  $\text{Cu}_3\text{Sn}$ . Frequency domain thermoreflectance (FDTR) and electron backscatter diffraction (EBSD) were paired to measure the thermal conductivity and orientation of grains of an arc-melted  $\text{Cu}_3\text{Sn}$  ingot. The direct mapping of small grain ( $\sim 400$   $\mu\text{m}$ ) thermal conductivities to crystallographic orientations is challenging and has only been done once before [26]. Density functional theory and maximally localized Wannier functions were coupled to probe the anisotropy of the material's thermal and electrical transport. The tenfold  $\text{Cu}_3\text{Sn}$  superstructure proved to be prohibitively large for a direct *ab initio* calculation of these properties and was approximated systematically with a set of smaller structural models. The combined experimental and computational results indicate that the compound's intrinsic anisotropy is considerably smaller (1.15–1.24) than previously thought (2.8). The revised knowledge may improve the use of  $\text{Cu}_3\text{Sn}$  not only as an electronics packaging material but also as a 3D printed material [27–29] or a cost-effective metallic oxidation catalyst [30,31]. Given the difficulty of measuring or calculating transport anisotropy and the general paucity of such data on intermetallic compounds, the presented analysis may also be helpful for constructing simple descriptors [32] to predict transport properties based on easily accessible structural, electronic, or vibrational features.

## 2. Methods

### 2.1. Sample preparation

Pure  $\text{Cu}_3\text{Sn}$  was formed by arc-melting stoichiometric proportions of Cu and Sn wire (99.999% metals basis, ESPI Metals) on a water-cooled Cu hearth in a Ti-gettered argon atmosphere. After an initial melting of the wire, the resulting ingot (24.97% Sn, 75.03% Cu) was turned on its side and re-melted four times to ensure complete mixing. It was then heat-treated in a forming gas environment (95% Ar, 5%  $\text{H}_2$ ) at 898 K for 30 days to improve chemical homogeneity and relieve stresses. The ingot was ground and polished with a final step of colloidal silica (0.02  $\mu\text{m}$ ).

### 2.2. Material characterization

X-ray diffraction (XRD) was used to identify the phase of the arc-melted sample. The sample was converted to powder with a file. The  $2\theta$ - $\omega$  scan with a copper source ( $\text{Cu K}\alpha$ ) was performed in a Malvern Panalytical X'Pert PRO XRD system.

The polished sample was imaged optically (Zeiss Axio Imager M1m) and by scanning electron microscopy (SEM) (Zeiss Field Emission SEM, Supra 55 VP). Electron backscatter diffraction (EBSD) was used to identify the orientation of each imaged grain. In the EBSD measurements, Kikuchi patterns were collected every 7.5  $\mu\text{m}$  across the surface and compared with calculated patterns using the crystallographic data provided by [11] under a potential of 25 kV with a 12 mm working distance (EDAX DigiView). The orientation of each grain was calculated by taking a 10-point average of the output from positions near the center of each grain. Data from highly spotted grains were excluded from further interpretation.

Grains oriented near their principal orientations were prepared for transmission electron microscopy (TEM) (JEOL High-resolution

TEM JEM 2100F) by focused-ion beam milling (FIB) (FEI Nova 600 Nanolab). TEM characterization validated the crystal structure anti-phase periodicity and the EBSD determined orientations. FDTR and EBSD mappings were performed to establish the orientation-dependent thermal conductivity of each grain.

### 2.3. Thermal conductivity measurements

Local thermal measurements were performed via FDTR mapping [33–36]. Our FDTR experimental setup employs a periodically modulated pump operating at 488 nm that periodically heats the sample. A coaxial probe laser measured the temperature via thermoreflectance using a continuous wave laser at 532 nm. The pump and probe beams were focused with a 20X objective (Mitutoyo Plan-Apochromat, 0.42 NA, 20 mm WD) to 3.2 and 2.9  $\mu\text{m}$   $1/e^2$  radii beams, respectively. At each location, thermal phase measurements were taken at 13 logarithmically-spaced frequencies ranging from 15 kHz to 2.6 MHz.

A two-parameter fit of the thermal diffusion model provided simultaneous extraction of the thermal conductivity of the  $\text{Cu}_3\text{Sn}$  layer and the interfacial resistance between the Au film and the  $\text{Cu}_3\text{Sn}$  layer. In this material system, the Au-oxide and oxide- $\text{Cu}_3\text{Sn}$  interfaces were grouped and approximated as a single interfacial layer. The oxide film was estimated to be  $\sim 2$  nm in thickness based on the work of Cho et al. [37], in which TEM was used to measure the oxide thickness formed on  $\text{Cu}_3\text{Sn}$  nanoparticles. The thickness of each grain in the  $\text{Cu}_3\text{Sn}$  ingot was estimated to be much larger than the thermal diffusion length at the lowest measurement frequency and consequently was treated as a semi-infinite terminating layer. The volumetric heat capacity of  $\text{Cu}_3\text{Sn}$  has previously been reported [38] and was input as a fixed parameter in this analysis. A bulk thermal conductivity measurement was performed with flash diffusivity (Anter Flashline 2000). The absolute uncertainty of a single thermal conductivity measurement was calculated to be  $\sim 1.7$   $\text{W}/\text{m}\cdot\text{K}$ . This was determined by propagating uncertainties  $\Delta\kappa_i$  for each input parameter  $i$  and then combining them orthogonally:  $\Delta\kappa_{\text{Cu}_3\text{Sn}} = \sqrt{\sum_i \Delta\kappa_i^2}$ . Table S1 in the Supplementary Material compiles the  $\Delta\kappa_i$ , along with detailed experimental uncertainty analysis.

To construct a thermal map using FDTR, a three-axis motorized translation stage (Thorlabs PT3 Z8) was employed during imaging experiments to scan the laser across the sample surface in a  $78 \times 242$  grid with 20  $\mu\text{m}$  increments. Measurements were performed near room temperature with a steady-state temperature rise of less than 10 K.

### 2.4. Stability and thermal conductivity calculations

Our density functional theory (DFT) analysis was performed in the generalized gradient approximation [39] with the Perdew-Burke-Ernzerhof exchange correlation functional [40]. Unless specified otherwise, we used VASP [41,42] with the projector augmented wave potentials [43] and a 500 eV energy cutoff. Select structures were also evaluated in the local density functional approximation (LDA) [44]. Vibrational entropy contributions to the free energy were evaluated for supercells with 128 atoms using the frozen phonon method implemented in Phonopy [45].

Electron transport coefficients were evaluated (i) in the constant relaxation time approximation (CRTA) with maximally localized Wannier functions using the Wannier90 code [46] and the Boltzmann module [47]; and (ii) in the relaxation time approximation (RTA) using the Electron-Phonon Wannier (EPW) package [48,49]. For the latter, we used the QUANTUM ESPRESSO package [50] with norm-conserving pseudopotentials and a 90 Ry energy cutoff. The formalism and the settings are described further in the corresponding sections.

Lattice transport for the smallest representative structure was calculated at the DFT level in the single-mode relaxation-time approximation and a full solution of the linearized phonon Boltzmann equation as implemented in Phono3py [51]. The lattice transport coefficients for larger structures were evaluated with Phono3py and a neural network (NN) interatomic potential. The NN was constructed with our MAISE-NET protocol [52], which generates reference data and optimizes adjustable parameters in an iterative fashion. We started with previously developed Cu and Sn NN potentials [52] and built a binary Cu-Sn model using our stratified training approach [53]. The 145–10–10–1 Behler-Parrinello NN model with 1880 adjustable parameters fitted to 7685 energy data and 69,579 atomic force data had a root mean square error of 9.5 meV/atom.

In order to reduce the numerical noise due to the  $k$ -point sampling and plane-wave expansion in the DFT calculations of relative stability, we used 64-atom orthorhombic representations of all structures (except for the tenfold model) with the same  $12 \times 2 \times 16$  k-mesh. The observed numerical errors were found to be in the 0.2–0.4 meV/atom range. The  $a = 5.526$  Å,  $b = 48.519$  Å, and  $c = 4.318$  Å lattice constants of the tenfold superstructure fully optimized in our DFT calculations were within 0.02, 1.5, and 0.03% of Müller and Lidin's values. Full structural information for the most relevant configurations considered in this study is given in the Supplementary Material.

### 3. Results and discussion

#### 3.1. XRD

As shown in Fig. 1, the powder x-ray diffraction (XRD) corresponds with the literature [11], confirming a pure single phase of  $\text{Cu}_3\text{Sn}$ . Lattice constants calculated from this experiment agreed within 0.2% of Müller and Lidin's lattice spacing of  $a = 5.520$  Å,  $b = 47.790$  Å, and  $c = 4.333$  Å. These dimensions indicate a tenfold repeating superstructure that agrees with the TEM analysis performed on grains calculated to have orientation near or at principal orientations of the  $\text{Cu}_3\text{Sn}$  crystal structure.

#### 3.2. Thermal conductivity mapping

Fig. 2 displays the optical image, the raw EBSD Inverse Pole Figure (IPF), and the FDTR thermal conductivity map of the probed area. The IPF displays orientations relative to the sample surface.

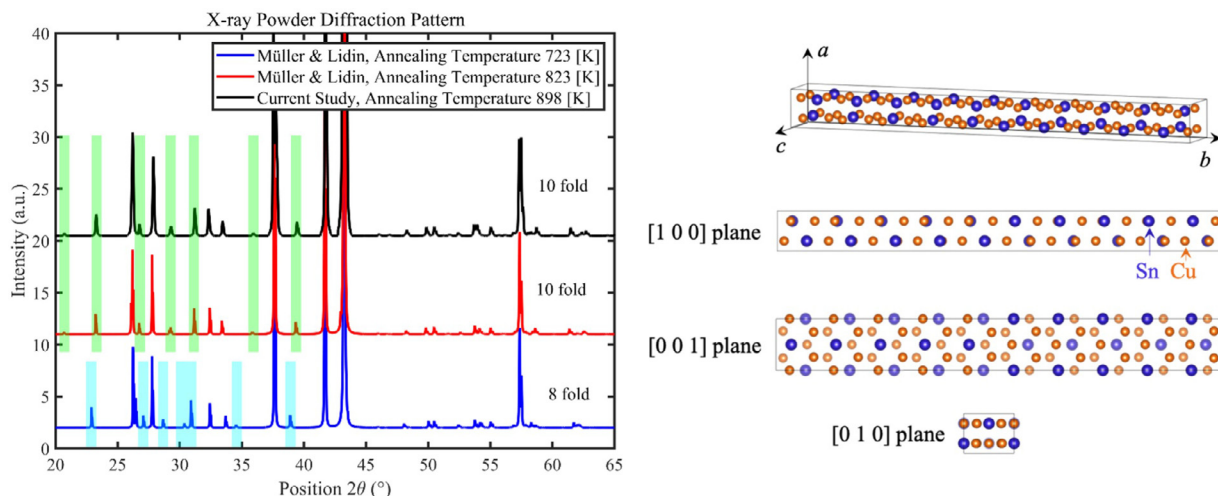


Fig. 1. Raw powder XRD diffraction pattern shows excellent agreement with spectra based on Müller and Lidin's annealed at 823 K (tenfold superlattice unit cell) crystallographic data [11]. No peaks for the eightfold structure were detected. Inset:  $\text{Cu}_3\text{Sn}$  tenfold superlattice unit cell and the projected images of each principal plane.

Grains were numbered using the EBSD IPF. Indeterminate orientations were observed for a few grains (e.g., 38, 114), as the backscatter detector size was too small to uniquely identify the crystal orientation from the Kikuchi pattern [54].

Fig. 3 displays the TEM images of grains #15 and #62. These grains were chosen because their EBSD orientations were near principal axes. TEM analysis revealed a crystal structure composed of a tenfold repeating superlattice for both grains and the calculated orientations were in good agreement with the EBSD measurements (see Fig. S1 for details on the electron diffraction pattern analysis).

Pixel analysis of the thermal image provided representative thermal conductivity values for each grain. As an aid in this process, grain boundaries observed in the optical image were overlaid onto the thermal image. The perimeter of a grain was traced, producing a binary map where the intensities of the pixels inside the traced area were saved, while all pixels outside the trace were ignored. This process was repeated for each grain. To reduce the effect of outliers on the average grain conductivity, a normal distribution was fit to the pixel intensity histogram distribution of each grain. Fig. 4a and b show the statistical distribution of thermal conductivities in grains #15 and #104. The fits for locations indicated in Fig. 2c are shown in Fig. 4c and d for grains #15 and #104.

The effect of crystal orientation on thermal conductivity is shown in Fig. 5. In this representation, orientation and conductivity pairs were plotted, where the direction from the origin represents the crystallographic orientation and the magnitude of the vector represents the thermal conductivity in that direction. An ellipsoid surface was then fit to the orientation and conductivity pairs using a least-squares regression enabling visualization of the thermal conductivity for any prescribed orientation [55]. Intersections of the ellipsoid with each axis represent the thermal conductivity parallel to each principal axis of  $\text{Cu}_3\text{Sn}$ 's crystal structure. The standard deviation of the ellipsoid fit residuals is less than 0.3 W/m-K.

Our measured bulk thermal conductivity value of 62.5 W/m-K falls within the measured directional conductivity range. However, this value is closer to the upper conductivity limit. This is likely due to a preferred grain directionality along the  $c$ -axis within the ingot. The flash diffusivity bulk thermal conductivity measurement agreed well with the literature [38]. The reported average of  $R_f \sim 3.5 \times 10^{-8}$  K m<sup>2</sup>/W in this study was comparable with previously reported values for thermal resistance through thin metal-oxide films [56–58].

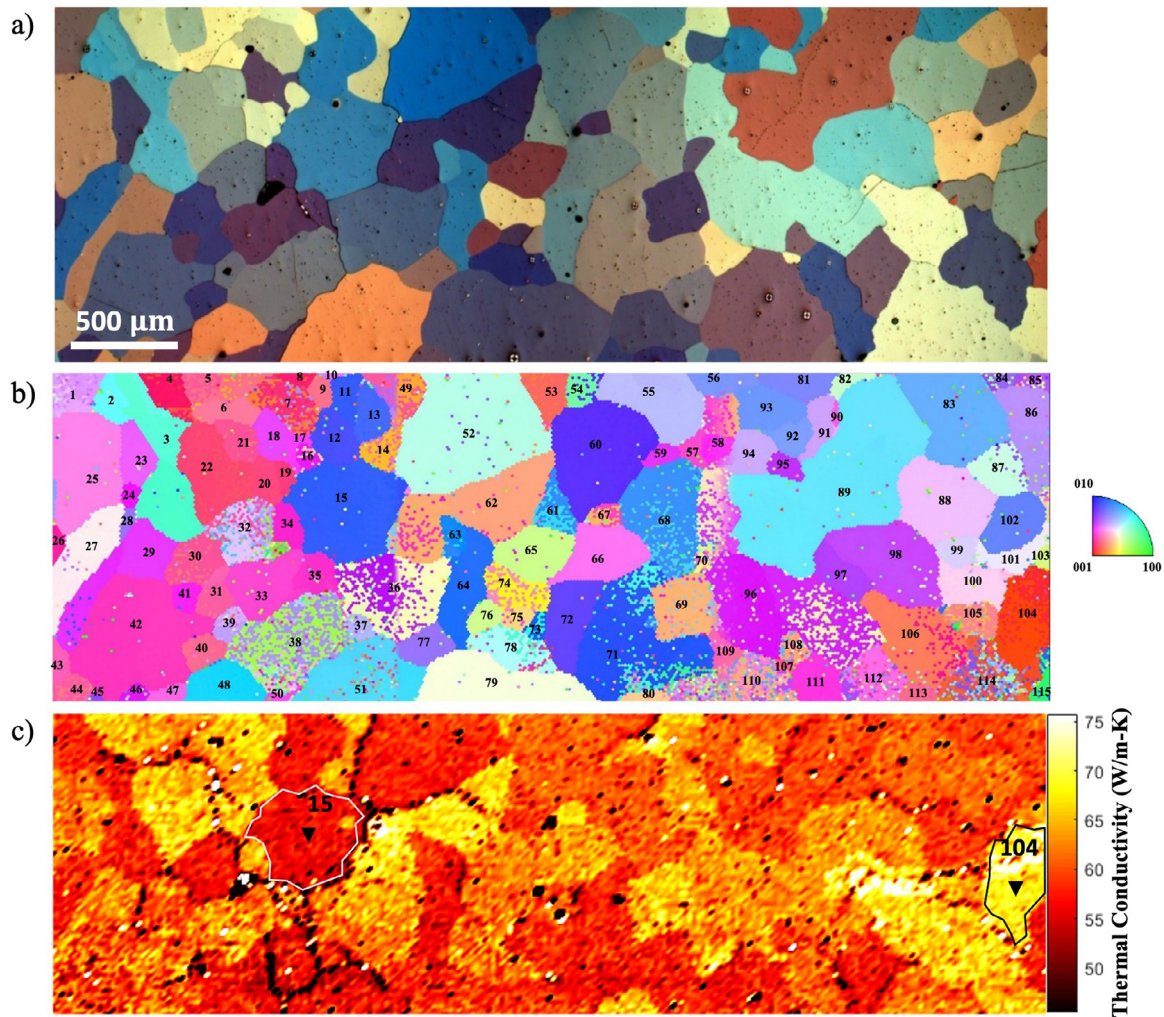


Fig. 2. Side-by-side comparison of the (a) optical, (b) orientation, and (c) thermal conductivity images.

In intermetallic alloys at room temperature, heat is transported primarily by electrons, and conversion between thermal and electrical conductivity can be done with the Wiedmann-Franz law,  $\sigma = L\kappa T$ , where  $\sigma$  is the electrical conductivity,  $\kappa$  is the thermal conductivity,  $T$  is the temperature, and  $L$  is the Lorentz number [59]. A universal constant of  $2.44 \times 10^{-8} \text{ W}\Omega\text{K}^{-2}$  for  $L$  is typically used for pure metals and some alloys [60]. However, some divergence from this constant is common among intermetallic alloys [59].

Only two other studies have looked at the thermal [38,10] or electrical [10] transport in  $\text{Cu}_3\text{Sn}$ , and neither measured the anisotropic thermal conductivity. To compare all available transport data, we converted the anisotropic electrical conductivity measured by Liu et al. [10] to the corresponding thermal conductivity values using the orientation-averaged Lorentz parameter  $L = 2.07 \times 10^{-8} \text{ W}\Omega\text{K}^{-2}$  from Ref. [38]. Table 1 illustrates notable differences in the three sets of results obtained on gas atomized [38], liquid-phase electroepitaxial [10], and arc-melted (this study)  $\text{Cu}_3\text{Sn}$  samples. The slightly higher (11%) bulk value measured by Frederickse et al. [38] compared to ours can be attributed to differences in the microstructures (deviations in stoichiometry can also lead to sizable thermal conductivity changes in intermetallic compounds [61–63], but  $\text{Cu}_3\text{Sn}$  has a narrow range of allowed compositions [11]). The much lower conductivities and much higher anisotropy ratio of Liu et al. [10] may have been caused by the unique sample processing method employed in that

Table 1

Literature comparison of the thermal conductivity of  $\text{Cu}_3\text{Sn}$ . The asterisked thermal conductivities represents the thermal conductivity estimated from electrical conductivity based on the Wiedmann-Franz law. A comparison based on crystallographic directions is not possible because Liu et al. did not report orientation-resolved conductivities.

$\kappa$ (W/m-K)	This work	Liu et al. [10]	Frederickse et al. [38]
Min	57.6	15.53*	–
Max	67.2	44.03*	–
Bulk	62.5	–	70.4
Ratio	1.17	2.83*	–

work. The liquid-phase electroepitaxy process applies a large current that could induce anisotropy, non-stoichiometric forms, grain boundaries, and defects. Unfortunately, we could not establish the precise reason for the discrepancy between our and Liu et al.'s findings because crystallographic orientation-resolved conductivities, microstructure, and microscopy data were not reported.

### 3.3. Crystal structure analysis

Several crystal structure solutions have been considered for  $\text{Cu}_3\text{Sn}$  over the last century [11,12,64–67]. The widely accepted model proposed by Wantanabe et al. in 1983 [12] is a tenfold superstructure based on the  $\text{Cu}_3\text{Ti}$  lattice, although eightfold superstructures had also been reported [67]. In 2014, Müller and

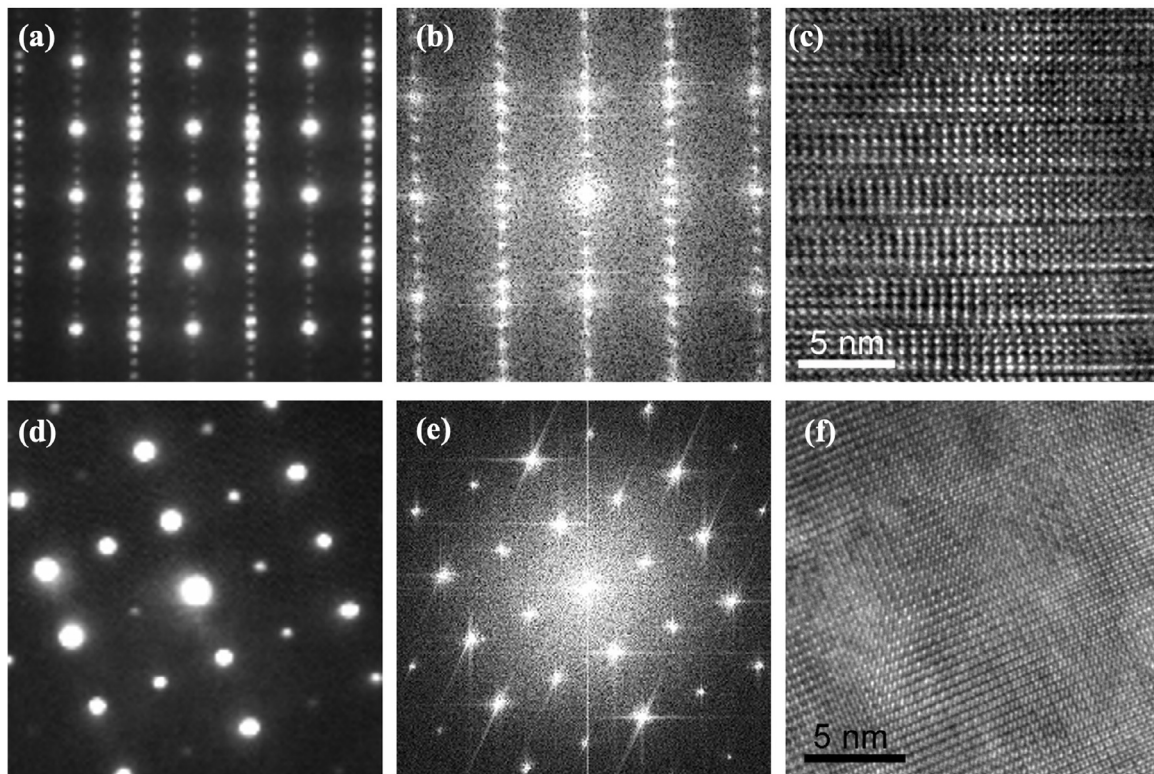


**Fig. 3.** TEM analysis of two neighboring grains shown in Fig. 2: (a–c) grain #15 and (d–f) grain #62. (a,d) The electron diffraction pattern; (b,e) the fast Fourier transform patterns from (c,f); and (c,f) the high resolution TEM (HRTEM) images. Panel (c) clearly shows a tenfold superlattice. The orientations of the grains #15 and #62 correspond to  $[0\ 1\ 0]$  and  $[1\ -5\ 1]$  zone axes of the tenfold  $\text{Cu}_3\text{Sn}$  superlattice, respectively.

Lidin found that the eight- and tenfold structures never appeared in samples together and that the formation of the particular superstructure had no clear correlation with either composition or annealing temperature [11]. These authors proposed a new off-stoichiometry modulated structure model that successfully accounted for the absence of even-order reflections in XRD patterns. In 2009, Sang et al. observed a different phase of  $\text{Cu}_3\text{Sn}$ , determined with electron diffraction and HRTEM to have a much simpler  $\text{DO}_{19}$  structure [66].

In this work, we employed DFT calculations detailed in Section 2.4 to investigate the stability of the competing models with respect to the structural and compositional modulations at different temperatures. Structural modulations were studied by considering supercells with different stackings of basic 8-atom  $\text{Cu}_3\text{Ti}$  units along the  $b$  axis and, correspondingly, different numbers of anti-phase boundaries (APBs). Two structures, representing the extremum cases, served as reference points for comparison, whereas intermediate phases were used to approach the large-size eight- and tenfold structures known experimentally. The phase with no APBs, denoted as  $|0\rangle$ , has a single  $\text{Cu}_3\text{Ti}$  unit ( $\text{DO}_a$ ). The phase with the maximum number of APBs along the  $b$  axis, denoted as  $|01\rangle$ , consists of one direct and one inverted  $\text{Cu}_3\text{Ti}$  units; this stacking is the hexagonal  $\text{P6}_3/\text{mmc}$   $\text{Ni}_3\text{Sn}$  prototype ( $\text{DO}_{19}$ ) in an orthorhombic representation.

Fig. 6a shows the  $\text{Cu}_3\text{Sn}$  stability at zero temperature as a function of the number of APBs. Interestingly, we found the  $|01\rangle$  structure to be notably more stable than  $|0\rangle$  by 2.3 meV/atom and any of the eight- or tenfold superstructures by  $\sim 1.2$  meV/atom. The energy differences were found to be not very sensitive to the DFT flavor, as we observed similar respective values, 2.8 meV/atom and  $\sim 1.7$  meV/atoms, at the LDA level. Therefore, the observed approximately linear dependence of the relative stability on the number of APBs in Fig. 6a indicates that the boundaries have a persistent

stabilizing effect in these DFT calculations. Qu et al. [68] have recently published DFT results on the cohesive and formation energies of competing  $\text{Cu}_3\text{Sn}$  phases but the proposed order of stability appears to have been based on unphysically large energy differences<sup>4</sup>.

The established favorability of the previously synthesized  $\text{DO}_{19}$  phase [66] in our DFT calculations at zero temperature suggests that the formation of the long-period  $\text{Cu}_3\text{Sn}$  superstructures could be promoted by temperature-dependent thermodynamic and/or kinetic factors. For thermodynamic stability analysis of relevant structures at elevated temperatures, we calculated free energy contributions arising from the vibrational and configurational entropies.

In order to resolve sub-meV/atom free energy differences on account of phonons, we used supercells with the same number of atoms and similar dimensions as described in Fig. S2. Converged results obtained for the  $|0\rangle$ ,  $|0011\rangle$ , and  $|01\rangle$  structures reveal only minor changes in the relative free energies that further favor the  $|01\rangle$  phase: by 0.2 meV/atom and 0.7 meV/atom at 900 K with respect to  $|0011\rangle$  and  $|0\rangle$ , respectively (hollow points in Fig. 6a).

Examination of the possible stabilization effect due to compositional modulation involved simulations of substitutional defects in the  $|0\rangle$ ,  $|000011111\rangle$ ,  $|0011\rangle$ , and  $|01\rangle$  superstructures with 64 atoms. We chose this cell size to probe  $\text{Cu}_{3+y}\text{Sn}$  stoichiometries around  $y = 0.16$  reported experimentally [11], as one Sn substitution with Cu corresponds to  $x \approx 0.234$  or  $y = (1-4x)/x \approx 0.27$ . Since the con-

<sup>4</sup> The reported cohesive energies of  $-3.949$  eV/atom for  $|0\rangle$ ,  $-3.271$  eV/atom for  $|01\rangle$ , and  $-4.426$  eV/atom for  $|0000011111\rangle$  [68] result in  $\Delta E_{|01\rangle-|0\rangle} = 678$  meV/atom and  $\Delta E_{|01\rangle-|0000011111\rangle} = -477$  meV/atom. These energy differences are orders of magnitude larger than typical relative energies for phases with close morphologies and well beyond typical systematic/numerical errors in DFT calculations. For example, using the  $k$ -meshes specified in Ref. [68], we obtained  $\Delta E_{|01\rangle-|0\rangle} = -2.2$  meV/atom, consistent with our value of  $-2.3$  meV/atom.

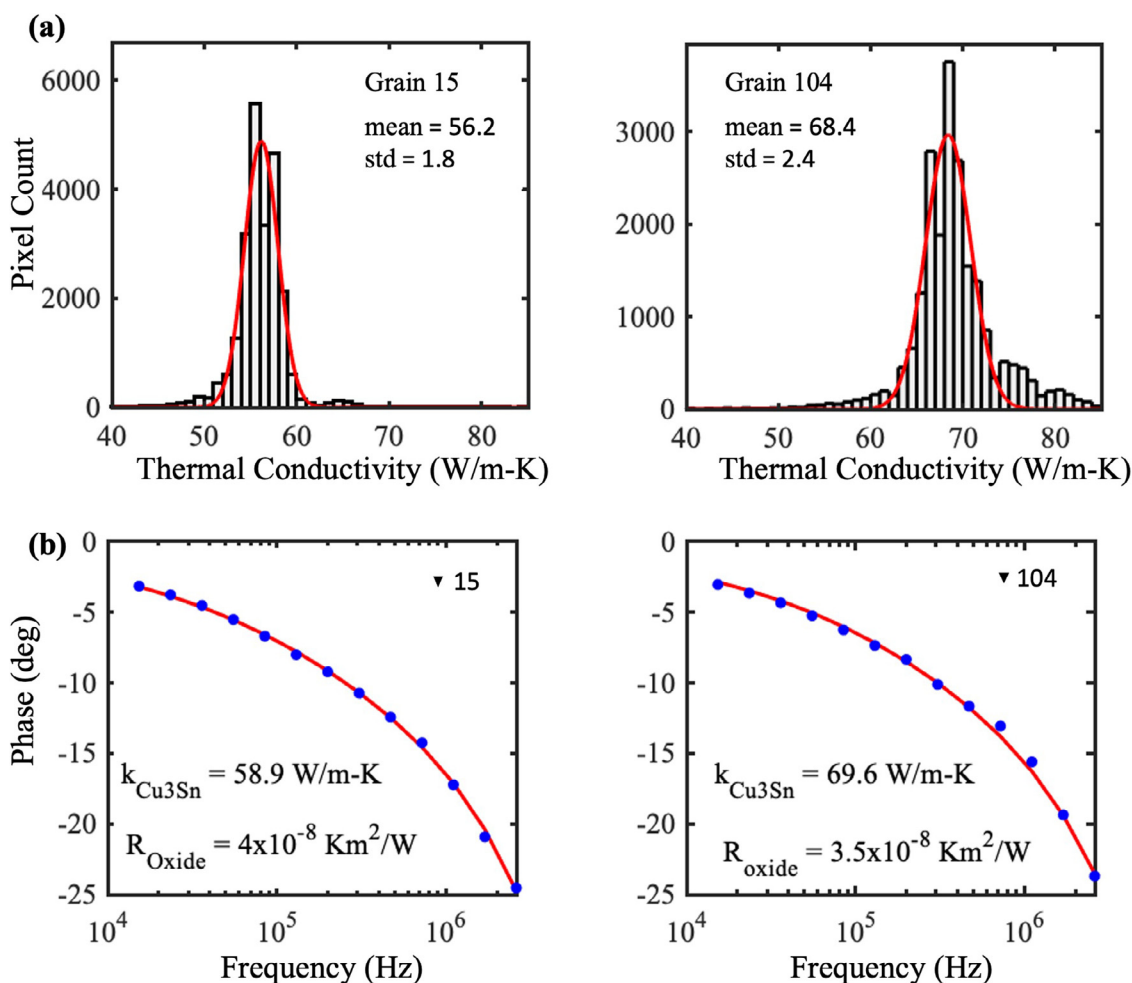


**Fig. 4.** (a) Thermal conductivity histograms corresponding with traced outlines from Fig. 2. (b) Measured phase and best fit of the locations indicated in Fig. 2. The image analysis is from an upsampled image, with  $\sim 50$  pixels equaling one thermal measurement.

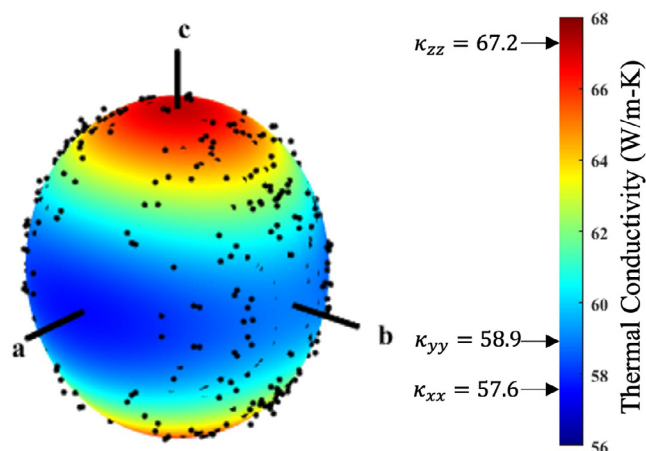


**Fig. 5.** Surface representation of the thermal conductivity variation with orientation. The measured data was reflected into each quadrant in an effort to show the alignment between the data and conductivity ellipsoid.

considered models have 1, 4, 2, and 1 non-equivalent Sn sites, respectively, we obtained between 1 and 4 defect energies per structure ranging between 0.24 and 0.33 eV/defect (see Fig. S3). Fig. 6b summarizes the free formation energies with respect to the Cu  $\leftrightarrow$  [01]-Cu<sub>3</sub>Sn tie-line calculated at zero and elevated temperatures. We

used the standard  $F_{\text{conf}} = k_B T [x_d \ln x_d + (1 - x_d) \ln(1 - x_d)] + x_d E_d$  expression, which works well in materials with a single defect energy value  $E_d$  and a small effective interaction between defects at concentration  $x_d$ . The relative free energy curve for [01] calculated at 900 K indicates that the range of stability extends down to  $x = 0.246$  ( $y \approx 0.065$ ), in good agreement with the experimental analysis [11]. The assessment of the configurational entropy term for [0011] and [00001111] is more complicated because the structures have 2 and 4 different values of the defect energies, respectively. Based on Refs. [69,70],  $F_{\text{conf}}$  for low concentrations of weakly interacting defects can be evaluated to first order as  $k_B T [x_d \ln x_d + (1 - x_d) \ln(1 - x_d)] - k_B T x_d \ln(\frac{1}{K} (\sum_{k=1}^K e^{-E_d^k/k_B T}))$ , where  $E_d^k$  is the defect formation energy associated with each of the  $K$  non-equivalent defects. The free formation energy curve at 900 K for [00001111] is shown in Fig. 6b in red. The configurational entropy contribution reduces the zero-temperature 1.2 meV/atom free formation energy gap between [00001111] and [01] by no more than 0.2 meV/atom at 900 K, which, at best, only offsets the estimated 0.2–0.7 destabilization effect due to the vibrational entropy. We also examined the possibility of obtaining off-stoichiometry phases with  $x > 0.25$  by calculating defect energies for substituting Cu with Sn. As can be seen from the steep curves in Fig. 6b, the stability range to the right is expected to be negligible even at high temperatures.

These findings indicate that the long-period superstructures are not high-temperature ground states. Their formation may be de-

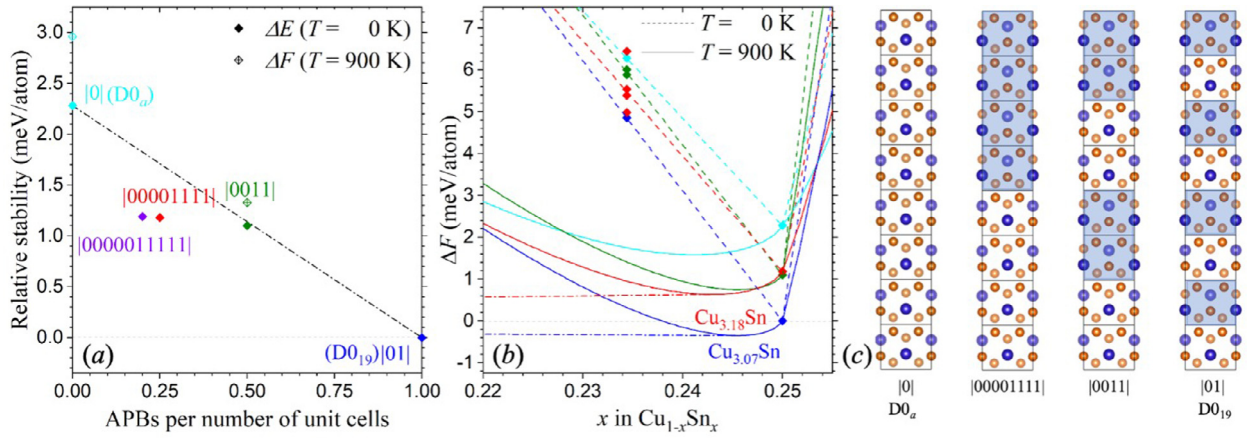


**Fig. 6.** (a) Relative stability of  $\text{Cu}_3\text{Sn}$  phases with the vibrational entropy contribution at 900 K (hollow points) and without it (solid points) as a function of the number of APBs per two 8-atom units. The line connecting the endpoints is a guide for the eye. (b) Relative free energy for off-stoichiometry structures with respect to Cu and  $|01\rangle$ - $\text{Cu}_3\text{Sn}$ . The points at  $x \approx 0.234$  correspond to 64-atom superstructures with one substitutional defect, the dashed (solid) curves show approximated free energies at 0 K (900 K), the dot-dash lines are tangents to the free energy curves, and the color-coding is shown in panel (a). (c) Illustration of  $\text{Cu}_3\text{Sn}$  superstructures, with the inverted  $\text{Cu}_3\text{Ti}$  units shaded in blue.

terminated by the kinetics of the phase nucleation and annealing processes that are beyond the scope of *ab initio* simulations. Experimentally, the annealing time has been shown to affect the size of APB domains in  $\text{D0}_{19}$ -based alloys [71,72]. Due to the difficulty of comparing the details of sample preparation procedures from different studies, further systematic investigation is needed to establish how the synthesis conditions influence the formation of the particular  $\text{Cu}_3\text{Sn}$  phases.

It is worth acknowledging that there is a generally good agreement between common DFT approximations and experiments regarding ground state crystal structures in metal alloys and intermetallics [73,74]. While accurate evaluation of formation energy magnitudes does require specific functionals in some cases [75,76], the description of relative energies for similar structures is more reliable due to the cancelation of errors. In particular, our previous DFT calculations have helped (i) revise misidentified structures of  $\text{CrB}_4$  [77,78],  $\text{MnB}_4$  [73], and  $\text{Na}_2\text{IrO}_3$  [79]; (ii) guide the discovery of new LiB [80,81],  $\text{CaB}_6$  [82],  $\text{FeB}_4$  [83,84], and  $\text{NaSn}_2$  [81] materials; and (iii) reproduce and explain the shifts in stoichiometry in the known  $\text{Na}_{1+x}\text{Sn}_2$  [85] and  $\text{LiB}_x$  [86] compounds.

### 3.4. First principles calculations of the thermal conductivity

*Ab initio* calculation of the  $\text{Cu}_3\text{Sn}$  transport properties presents a considerable challenge due to the size of the experimentally established structures. In view of the recent work on related materials [87,88] and our tests on representative  $\text{Cu}_3\text{Sn}$  structures, we find the following approximations suitable for handling large systems and reliable for estimating the transport anisotropy in this compound.

First, we examined the lattice contribution to thermal transport. A recent systematic *ab initio* analysis of metals with simple structures [87] revealed that phonons can be responsible for up to 41% of the total thermal conductivity at room temperature. In order to obtain an upper bound for the lattice transport, we calculated the phonon-phonon relaxation time due to three-phonon scattering. Evaluation of third-order force constants requires a larger number of displacements, e.g., 2621 for the  $2 \times 2 \times 2$  supercell of the smallest 8-atom  $|0\rangle$  phase, and becomes prohibitively expensive at the DFT level for bigger structures.

Table 2 demonstrates that the lattice thermal conductivity contribution calculated with DFT for  $|0\rangle$  is below 1.5 W/m-K, which is less than 2.5% of the measured thermal conductivity. We also evaluated this term using a NN interatomic potential and observed a

**Table 2**

Phonon-phonon contribution to the thermal conductivity (in W/m-K) calculated at 300 K with the density functional theory (DFT) and a neural network (NN) interatomic potential for different  $\text{Cu}_3\text{Sn}$  structures.

method	structure	$\kappa_{xx}$	$\kappa_{yy}$	$\kappa_{zz}$
DFT	$ 0\rangle$	0.99	0.74	1.45
NN	$ 0\rangle$	1.06	0.72	1.29
NN	$ 01\rangle$	0.82	0.82	1.79
NN	$ 0011\rangle$	0.65	0.57	1.08

good agreement with the DFT results (Table 2) even though the NN was not specifically fitted to the near-equilibrium  $\text{Cu}_3\text{Sn}$  configurations [52]. The significantly lower computational cost allowed us to check that the phonon-phonon contribution remains small for the  $|01\rangle$  and  $|0011\rangle$  representations. Since the inclusion of the phonon-electron scattering would further lower the lattice transport according to Matthiessen's rule [89] (e.g., in  $\text{Cu}_3\text{Au}$  it reduced the value from 2.37 W/m-K down to 1.89 W/m-K [87]), it is evident that the lattice thermal conductivity has a negligible effect on the full transport anisotropy in  $\text{Cu}_3\text{Sn}$ .

For evaluation of the electron transport properties, a common approach to solve the Boltzmann transport equations for large systems, typically with fewer than 32 atoms per unit cell and in some cases with up to 64 atoms per unit cell [90–95], relies on the CRTA and maximally localized wave functions (MLWFs). MLWFs provide a smooth interpolation of the band structure for obtaining the group velocities in the  $i$  and  $j$  directions in Eq. (1) for each band  $n$  at an arbitrary  $\mathbf{k}$ -point:

$$v_{i,n\mathbf{k}} = \frac{1}{\hbar} \frac{\partial E_{n\mathbf{k}}}{\partial k_i} \quad (1)$$

$$\Sigma_{ij}(\varepsilon) = \frac{1}{V} \sum_{n\mathbf{k}} v_{i,n\mathbf{k}} v_{j,n\mathbf{k}} \tau \delta(\varepsilon - E_{n\mathbf{k}}). \quad (2)$$

The transport function with a simple linear dependence on  $\tau$  in the CRTA (see Eq. (2) [47]) can now be calculated and used to determine thermoelectric transport properties. Eqs. (3)–(6) define  $K$ , the electrical conductivity  $\sigma$ , the Seebeck coefficient  $S$ , and the thermal conductivity  $\kappa$ :

$$K_{ij}(\mu, T) = \frac{1}{T} \int_{-\infty}^{+\infty} d\varepsilon \left( -\frac{\partial f(\varepsilon, \mu, T)}{\partial \varepsilon} \right) (\varepsilon - \mu)^2 \Sigma_{ij}(\varepsilon), \quad (3)$$

$$\sigma_{ij}(\mu, T) = e^2 \int_{-\infty}^{+\infty} d\varepsilon \left( -\frac{\partial f(\varepsilon, \mu, T)}{\partial \varepsilon} \right) \Sigma_{ij}(\varepsilon), \quad (4)$$

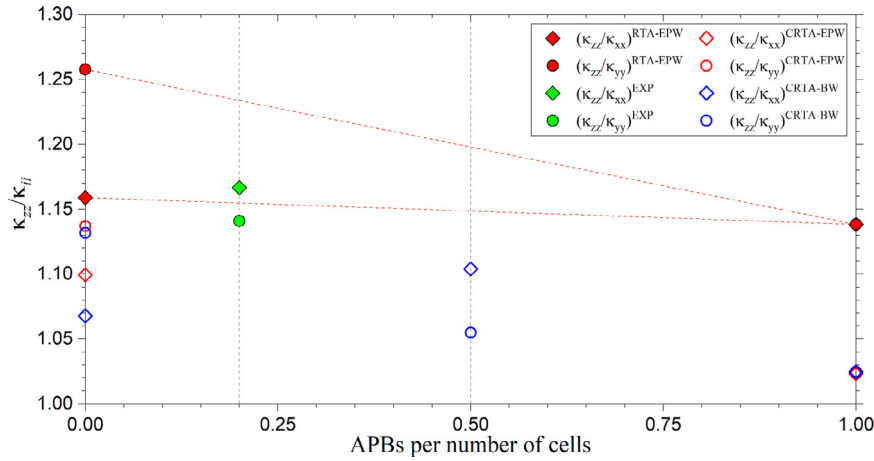


**Fig. 7.** Thermal conductivity ratios,  $\kappa_{zz}/\kappa_{xx}$  and  $\kappa_{zz}/\kappa_{yy}$ , for the experimental [0000011111] structure (solid green points) and the simulated [0], [001], and [01] models as a function of the number of APBs along the  $b$  axis per two 8-atom units. The solid red points correspond to the RTA results, while the hollow points show the CRTA results obtained with EPW (red) or Boltzmann (blue). The corresponding calculated electrical conductivity anisotropies are shown in Fig. S8. The linear interpolations shown as red dashed lines are a guide for the eye. At  $x=0.2$ , the minimum and maximum interpolated values are 1.155 and 1.233, respectively.

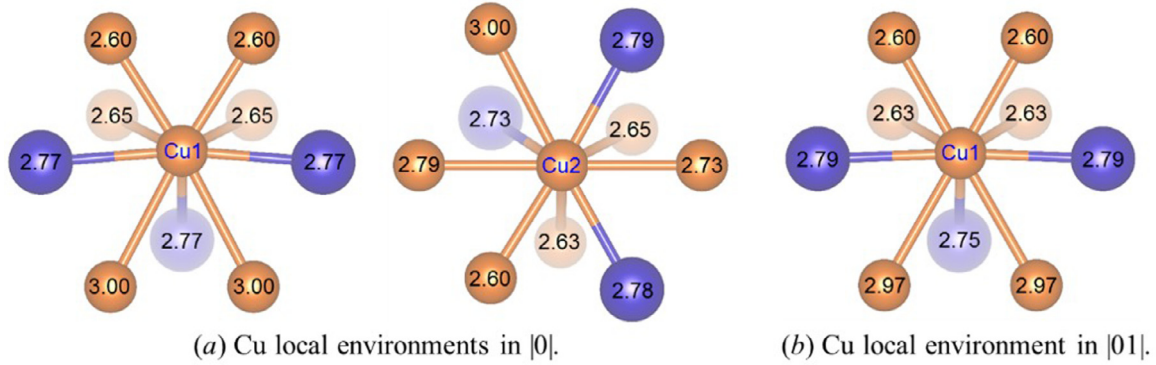


**Fig. 8.** Local atomic environments for Cu atoms in the [0] and [01] reference structures fully relaxed with DFT. The four Cu and two Sn neighbors in the  $x$ - $y$  plane are shown in orange and blue, respectively. The lighter shades denote two Cu and one Sn neighbors below the plane (an identical set above the plane is not shown for clarity). The interatomic distances from the central atom are given in Å.

$$S_{ij}(\mu, T) = \frac{e}{T\sigma_{ij}} \int_{-\infty}^{+\infty} d\varepsilon \left( -\frac{\partial f(\varepsilon, \mu, T)}{\partial \varepsilon} \right) (\varepsilon - \mu) \Sigma_{ij}(\varepsilon), \quad (5)$$

$$\kappa = \mathbf{K} - \mathbf{S}\sigma\mathbf{S}T \quad (6)$$

where  $f(\varepsilon, \mu, T)$  is the Fermi-Dirac distribution  $f(\varepsilon, \mu, T) = \frac{1}{e^{(\varepsilon-\mu)/k_B T} + 1}$ .

We started our analysis with the simple CRTA to examine the transport anisotropy arising from the  $k$ -dependence of the electronic band structure in different  $\text{Cu}_3\text{Sn}$  structural models. We constructed MLWFs with the Boltzmann module [47] of the Wannier90 software package [46] and observed converged values of the thermal conductivity anisotropy in the orthorhombic representations of the [0], [01], and [001] models for the disentanglement tolerance of  $10^{-7}$  (see Fig. S5) and the  $180 \times 90 \times 240$ ,  $180 \times 90 \times 240$ , and  $180 \times 45 \times 240$  interpolation meshes, respectively. The hollow blue points in Fig. 7 show that the  $\kappa_{zz}/\kappa_{xx}$  and  $\kappa_{zz}/\kappa_{yy}$  ratios in the CRTA are lower than the measured values. Namely, the [01] structure, with most APBs and identical  $\kappa_{xx}$  and  $\kappa_{yy}$  due to the symmetry of the hexagonal lattice, was found to have the least degree of thermal conductivity anisotropy, as the in-plane and out-of-plane values differed by only 2.5%. The reduction in the structural modulation leads to a more pronounced difference between the average in-plane and out-of-plane thermal conductivities: 7.9% in [001] and 10.0% in [0]. Within the plane, the sizable and non-monotonous changes in  $\kappa_{zz}/\kappa_{xx}$  and  $\kappa_{zz}/\kappa_{yy}$  indicate that a sim-

ple interpolation for intermediate structures might not capture the complex relationship between the transport anisotropy and the number of APBs. Note that the effective  $\tau$  of about 9 fs evaluated from the measured thermal conductivity (see Fig. S7) is close to the typical 10 fs value used in CRTA calculations [47].

In order to account for directional dependence of the electron-phonon coupling, one must go beyond the CRTA. In the RTA, the  $n\mathbf{k}$ -resolved scattering rate is obtained by integrating the square of the electron-phonon matrix elements  $|g_{mnv}(k, q)|$  over the phonon modes  $\mathbf{q}v$  as

$$\frac{1}{\tau_{n\mathbf{k}}} = \frac{2\pi}{\hbar} \sum_{mv\sigma} \int \frac{dq}{\Omega_{BZ}} |g_{mnv}(k, q)|^2 \times \left[ (1 + \sigma)/2 - \sigma f_{mk+q}^0 + n_{qv} \right] \delta(\Delta\varepsilon_{k,q}^{mn} - \sigma \hbar\omega_{qv})$$

where  $f_{n\mathbf{k}}^0$  is the equilibrium Fermi-Dirac distribution function,  $n_{qv}$  is the Bose-Einstein occupation, and  $\sigma = \pm 1$  indicates phonon absorption or emission. These  $\tau_{n\mathbf{k}}$  values are then used in the evaluation of the self-energy (Eq. (2)). Achieving convergence of transport properties in the RTA is far more demanding and only a handful of calculations have been performed for structures with above 10 atoms per unit cell [96–98]. Once we obtained well-behaving MLWFs with the combination of QUANTUM ESPRESSO and EPW (Fig. S4), a customized EPW version was employed to evaluate transport anisotropy. As a consistency check, we calculated  $\kappa_{zz}/\kappa_{xx}$  and  $\kappa_{zz}/\kappa_{yy}$  in the CRTA (hollow red points in Fig. 7) and observed a good agreement between the EPW and Boltzmann results for the

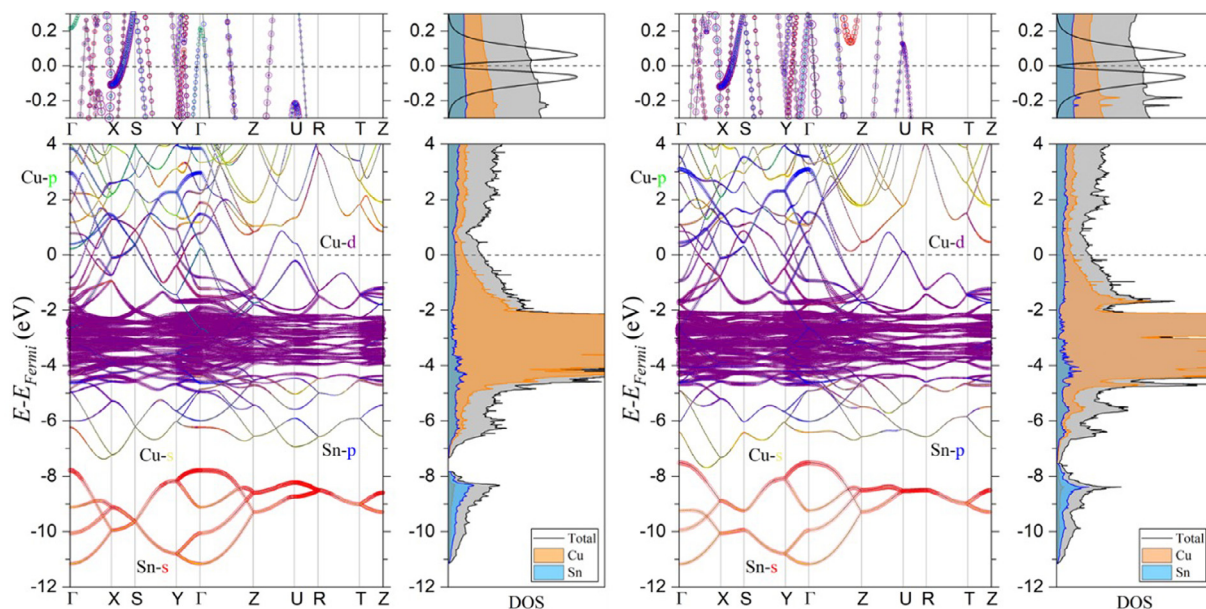


**Fig. 9.** Electronic band structure and density of states (DOS) for the  $|00|$  (left panels) and  $|01|$  (right panels) phases of  $\text{Cu}_3\text{Sn}$ . The electronic states are decomposed by orbital character in the band structure plots and by element in the DOS plots. The black lines in top DOS panels show  $-f'(\epsilon, \mu, T)(\epsilon - \mu)^2$  from Eq. (3) at  $T = 300$  K.

$|0|$  and  $|01|$  structures and comparable fine meshes. In our final RTA calculations,  $64^3$   $k$ - and  $q$ -meshes (Fig. S6) proved sufficient to ensure convergence of the thermal conductivity anisotropy estimates to within  $\sim 2\%$ . The solid red points in Fig. 7 illustrate that the  $k$  and  $q$  dependences of the electron-phonon scattering processes noticeably increase the ratios: from 1.10 to 1.16 for  $\kappa_{zz}/\kappa_{xx}$  and from 1.14 to 1.26 for  $\kappa_{zz}/\kappa_{yy}$  in  $|0|$ ; and from 1.02 to 1.14 for both ratios in  $|01|$ . The RTA results suggest that the  $\kappa_{zz}/\kappa_{xx}$  and  $\kappa_{zz}/\kappa_{yy}$  ratios for the eight- and tenfold structures would likely fall in the 1.15–1.24 range and would be in good agreement with the measured 1.14–1.16 values. The absolute  $(\kappa_{xx}, \kappa_{yy}, \kappa_{zz})$  thermal conductivities in the RTA ((106.1, 97.8, 122.9) W/m-K in  $|0|$  and (91.4, 91.4, 104.0) W/m-K in  $|01|$ ) are within 54–83% of the experimental values obtained in this work (absolute transport properties tend to converge more slowly than their ratios because they do not benefit from the cancelation of errors).

### 3.5. Analysis of atomic and electronic structures

In order to further investigate the dependence of the compound's bonding and transport properties on the presence of APBs, we examined the atomic environments (Figs. 8 and S5) and electronic features (Figs. 9, S3, S6, and S7) in all considered stoichiometric models paying special attention to the  $|0|$  and  $|01|$  endpoint structures.

The  $|0|$ ,  $|00001111|$ ,  $|0011|$ , and  $|01|$  HCP-based models share several morphological traits. They all have  $\text{Cu}_{12}$ -coordinated Sn sites with similar interatomic distances (2.7–2.8 Å) and  $\text{Cu}_8 + \text{Sn}_4$ -coordinated Cu sites with markedly different ranges of the in-plane (2.6–3.0 Å) and out-of-plane (2.6–2.7 Å) Cu-Cu distances. What distinguishes the models with different numbers of APBs is the distribution of the in-plane Cu-Cu distances within the 2.6–3.0 Å range: as shown in Figs. 9 and S5, the Cu1 sites in  $|0|$  and  $|01|$  have two short and two long bonds but the additional Cu2 site in  $|0|$  has one short, one long, and two intermediate-length bonds.

Likewise, the considered models share a number of common electronic structure features. The valence states in the  $(-11; -7.5)$  eV energy range have a dominant Sn-s character, the Cu-d states peak in the  $(-5; -1.5)$  eV range, and all Sn-s/p and Cu-s/d orbitals contribute to the hybridized states in the displayed range above

$-7.5$  eV. The subtle differences from the structural modulation are best illustrated with the  $|0|$  and  $|01|$  band structures (Fig. 9) calculated for similar 16-atom orthorhombic unit cells and along the same  $k$ -path see Fig. S10 [99]. In particular, the slightly different bandwidths, 3.4 in  $|0|$  and 3.7 eV in  $|01|$ , of the states centered around  $-9$  eV provide clues about the interplay between the Sn and Cu sublattices. While this dispersion is defined primarily by the Sn ss bond integrals centered on Sn atoms  $\sim 3.7$  Å apart, the hybridization between the low-lying Cu-s and the antibonding Sn-s states is significant: the bandwidth shrinks down to 2.4 eV in  $|0|$  and 2.8 eV in  $|01|$  if all Cu atoms are removed. For effective hybridization, the Cu-s states need to be dispersed significantly enough to become comparable in energy with the Sn-s states. As Fig. 9 shows, the two manifolds are separated by a 0.5 eV gap in  $|0|$  but have overlapping energies along  $\Gamma$ -Y in  $|01|$ . The features are consistent with  $|01|$  having a higher fraction of the short 2.6 Å Cu-Cu interatomic distances that cause a wider Cu-s bandwidth, which, in turn, contributes to the structure's higher stability.

The transport properties are defined primarily by the Cu-d and Sn-p states in the vicinity of the Fermi level shown with the double-peak curves in the DOS panels at the top of Fig. 9. The most significant difference between the  $|0|$  and  $|01|$  band structures in this energy window is observed along the  $\Gamma$ -Z-U-R directions. First, the lack of the crystal field splitting at the U point in  $|01|$  results in extra Cu-d-Sn-p bands crossing the Fermi level along Z-U and U-R. Second, the bottom edge of the Cu-s-Sn-s band near the Z point shifts from 0.8 eV in  $|0|$  down to just above 0.1 eV in  $|01|$  and these states start to contribute to thermal transport. Despite these beneficial features along these select high-symmetry directions in  $|01|$ , the MLWF-based integration over the full Brillouin zone in the CRTA showed overall higher thermal conductivity components (77.9, 73.5, 83.2) W/m-K in  $|0|$  compared to (75.3, 74.9, 77.0) W/m-K in  $|01|$  if the same constant  $\tau = 10$  fs was used for the two compounds (see Fig. S8).

## 4. Conclusions

$\text{Cu}_3\text{Sn}$  has promising applications in electronics packaging, additive manufacturing [27–29,100], and catalysis [30,31] for which knowledge of the thermal conductivity is important. The 1.14–1.16

thermal conductivity anisotropy measured in our arc-melted  $\text{Cu}_3\text{Sn}$  ingot and 1.15–1.24 values estimated for  $\text{Cu}_3\text{Sn}$  long-period superstructures with our DFT calculations are considerably lower than the 2.8 value observed previously in liquid-phase electroepitaxied samples [10]. The anisotropy of  $\sim 15\%$ , primarily between the out-of-plane and in-plane directions, is fairly modest for an HCP-based material. Simulation of several  $\text{Cu}_3\text{Sn}$  superstructures reveals that the presence of anti-phase boundaries can change the transport anisotropy by  $\sim 10\%$ . The DFT thermodynamic stability analysis suggests that the previously observed  $\text{D0}_{19}$  structure featuring the maximum number of anti-phase boundaries is the  $\text{Cu}_3\text{Sn}$  ground state in the relevant temperature range, which points to the importance of kinetic factors in the formation of the known long-period superstructures.

### Declaration of Competing Interest

The authors declare that they have no known competing financial interests or personal relationships that could have appeared to influence the work reported in this paper.

### Acknowledgments

S.N.S. and M.A.D. acknowledge support from NSF-1846157, Binghamton's IEEC NYS CAT, and the SRC CHIRP 2878.003. M.A.D. acknowledge support from NSF-1742056. E.D.S. and A.N.K. acknowledge the NSF support (Award No. DMR-1821815) and the Extreme Science and Engineering Discovery Environment computational resources [101] (NSF Award No. ACI-1548562, Project No. TG-PHY190024). E.D.S. and A.N.K. thank the EPW team, especially H. Paudyal and H. Lee, for helpful discussions.

### Supplementary materials

Supplementary material associated with this article can be found, in the online version, at doi:10.1016/j.actamat.2022.117671.

### References

- [1] S. Herat, Green electronics through legislation and lead free soldering, *CLEAN Soil Air Water* 36 (2) (2008) 145–151 Feb., doi:10.1002/clean.200700164.
- [2] L. Zhang, D. Wang, W. Tong, A numerical simulation study on wetting and bridging of SnAgCu solder liquid, in: Proceedings of the 10th Electronics Packaging Technology Conference, 2008, pp. 1347–1350, doi:10.1109/EPTC.2008.4763618. Dec..
- [3] N. Saunders, A.P. Miodownik. <https://doi.org/10.1007/BF03029299>.
- [4] C. Chen, D. Yu, K.N. Chen, Vertical interconnects of microbumps in 3D integration, *MRS Bull.* 40 (3) (2015) 257–263 Mar., doi:10.1557/mrs.2015.29.
- [5] D. Wang, A.C. Miller, M.R. Notis, XPS study of the oxidation behavior of the  $\text{Cu}_3\text{Sn}$  intermetallic compound at low temperatures, *Surf. Interface Anal.* 24 (1996) 127–132.
- [6] H.G. Tompkins, J.E. Bennett, J.A. Augis, T.M. Paskowski, Oxidation of  $\text{Cu}_3\text{Sn}$  and  $\text{Cu}_6\text{Sn}_5$  films in room air from 175 to 250°C, *J. Electrochem. Soc.* 130 (8) (1983) 1758–1762 Aug., doi:10.1149/1.12120087.
- [7] R. Labie, W. Ruythooren, K. Baert, E. Beyne, B. Swinnen, Resistance to electromigration of purely intermetallic micro-bump interconnections for 3D-device stacking, in: Proceedings of the International Interconnect Technology Conference, 2008, pp. 19–21, doi:10.1109/IITC.2008.4546913. Jun..
- [8] R. Agarwal, et al., Cu/Sn microbumps interconnect for 3D TSV chip stacking, in: Proceedings of the Proceedings 60th Electronic Components and Technology Conference (ECTC), 2010, pp. 858–863, doi:10.1109/ECTC.2010.5490698. Jun..
- [9] H.Y. Zhao, et al., Non-interfacial growth of  $\text{Cu}_3\text{Sn}$  in Cu/Sn/Cu joints during ultrasonic-assisted transient liquid phase soldering process, *Mater. Lett.* 186 (2017) 283–288 Jan., doi:10.1016/j.matlet.2016.10.017.
- [10] C.Y. Liu, et al., Epitaxial Cu–Sn bulk crystals grown by electric current, *Acta Mater.* 61 (15) (2013) 5713–5719 Sep., doi:10.1016/j.actamat.2013.06.014.
- [11] C.J. Müller, S. Lidin,  $\text{Cu}_3\text{Sn}$ -understanding the systematic absences, *Acta Crystallogr. Sect. B Struct. Cryst. Eng. Mater.* 70 (5) (2014) 879–887 Oct., doi:10.1107/S205252061401806X.
- [12] Y. Watanabe, Y. Fujinaga, H. Iwasaki, Lattice modulation in the long-period superstructure of  $\text{Cu}_3\text{Sn}$ , *Acta Crystallogr. B* 39 (3) (1983) 306–311 Jun., doi:10.1107/S0108768183002451.
- [13] X.Y. Pang, S.Q. Wang, L. Zhang, Z.Q. Liu, J.K. Shang, First principles calculation of elastic and lattice constants of orthorhombic  $\text{Cu}_3\text{Sn}$  crystal, *J. Alloy. Compd.* 466 (1–2) (2008) 517–520 Oct., doi:10.1016/j.jallcom.2007.11.095.
- [14] Q. Yin, F. Gao, Z. Gu, J. Wang, E.A. Stach, G. Zhou, Interface dynamics in one-dimensional nanoscale Cu/Sn couples, *Acta Mater.* 125 (2017) 136–144 Feb., doi:10.1016/j.actamat.2016.11.051.
- [15] B.A. Sanborn, P.B. Allen, D.A. Papaconstantopoulos, Empirical electron-phonon coupling constants and anisotropic electrical resistivity in hcp metals, *Phys. Rev. B* 40 (9) (1989) 6037–6044 Sep., doi:10.1103/PhysRevB.40.6037.
- [16] R.W. Powell, R.P. Tye, M.J. Woodman, The thermal conductivity and electrical resistivity of polycrystalline metals of the platinum group and of single crystals of ruthenium, *J. Common Met.* 12 (1) (1967) 1–10 Jan., doi:10.1016/0022-5088(67)90062-8.
- [17] P.S. Balog, R.A. Secco, High pressure and temperature behaviour of electrical resistivity of hcp metals Ti, Zr and Gd, *J. Phys. Condens. Matter* 11 (5) (1999) 1273–1287 Feb., doi:10.1088/0953-8984/11/5/014.
- [18] R.J. Stierman, et al., Magnetic susceptibility and electrical resistivity of electrotransport purified scandium single crystals from  $\approx 1$  to 300 K, *J. Magn. Magn. Mater.* 36 (3) (1983) 249–254 Apr., doi:10.1016/0304-8853(83)90122-1.
- [19] K. Ohta, et al., An experimental examination of thermal conductivity anisotropy in hcp iron, *Front. Earth Sci.* 6 (2018) 176 Nov., doi:10.3389/feart.2018.00176.
- [20] A. Bar-Cohen, J.D. Albrecht, J.J. Maurer, Near-junction thermal management for wide bandgap devices, in: Proceedings of the IEEE Compound Semiconductor Integrated Circuit Symposium (CSICS), 2011, pp. 1–5, doi:10.1109/CSICS.2011.6062454. Oct..
- [21] M. Garven, J.P. Calame, Simulation and optimization of gate temperatures in GaN-on-SiC monolithic microwave integrated circuits, *IEEE Trans. Compon. Packag. Technol.* 32 (1) (2009) 63–72 Mar., doi:10.1109/TCAPT.2008.2004586.
- [22] Y. Won, J. Cho, D. Agonafer, M. Asheghi, K.E. Goodson, Fundamental cooling limits for high power density gallium nitride electronics, *IEEE Trans. Compon. Packag. Manuf. Technol.* 5 (6) (2015) 737–744 Jun., doi:10.1109/TCPMT.2015.2433132.
- [23] B. Yang, P. Wang, A. Bar-Cohen, Thermoelectric mini-contact cooler for hot-spot removal in high power devices, in: Proceedings of the 56th Electronic Components and Technology Conference 2006, 2006, p. 6, doi:10.1109/ECTC.2006.1645775. pp.–.
- [24] T. Foulkes, J. Oh, P. Birbarah, J. Neely, N. Miljkovic, R.C.N. Pilawa-Podgurski, Active hot spot cooling of GaN transistors with electric field enhanced jumping droplet condensation, in: Proceedings of the IEEE Applied Power Electronics Conference and Exposition (APEC), 2017, pp. 912–918, doi:10.1109/APEC.2017.7930805. Mar..
- [25] Z. Huang, R.E. Jones, A. Jain, Experimental investigation of electromigration failure in Cu–Sn–Cu micropads in 3D integrated circuits, *Microelectron. Eng.* 122 (2014) 46–51 Jun., doi:10.1016/j.mee.2014.03.003.
- [26] D.H. Olson, et al., Anisotropic thermal conductivity tensor of  $\beta\text{-Y}_2\text{Si}_2\text{O}_7$  for orientational control of heat flow on micrometer scales, *Acta Mater.* 189 (2020) 299–305 May, doi:10.1016/j.actamat.2020.02.040.
- [27] A. Azizi, M.A. Daeumer, S.N. Schiffrès, Additive laser metal deposition onto silicon, *Addit. Manuf.* 25 (2019) 390–398 Jan., doi:10.1016/j.addma.2018.09.027.
- [28] A. Azizi, M.A. Daeumer, J.C. Simmons, B.G. Sannakia, B.T. Murray, S.N. Schiffrès, Additive laser metal deposition onto silicon for enhanced microelectronics cooling, in: Proceedings of the IEEE 69th Electronic Components and Technology Conference (ECTC), Las Vegas, NV, USA, 2019, pp. 1970–1976, doi:10.1109/ECTC.2019.00302. May.
- [29] P.C. Hsieh, C.H. Tsai, B.H. Liu, W.C.J. Wei, A.B. Wang, R.C. Luo, 3D printing of low melting temperature alloys by fused deposition modeling, in: Proceedings of the IEEE International Conference on Industrial Technology (ICIT), 2016, pp. 1138–1142, doi:10.1109/ICIT.2016.7474915. Mar..
- [30] A. Stolle, B. Ondruschka, I. Morgenthal, O. Andersen, W. Bonrath, Metallic short fibers for liquid-phase oxidation reactions, *J. Mol. Catal. Chem.* 335 (1–2) (2011) 228–235 Feb., doi:10.1016/j.molcata.2010.11.038.
- [31] R. Brüning, et al., Innovative catalysts for oxidative dehydrogenation in the gas phase-metallic short fibers and coated glass fabrics, *Chem. Eng. Technol.* 28 (9) (2005) 1056–1062 Sep., doi:10.1002/ceat.200500157.
- [32] S. Curtarolo, G.L.W. Hart, M.B. Nardelli, N. Mingo, S. Sanvito, O. Levy, The high-throughput highway to computational materials design, *Nat. Mater.* 12 (3) (2013) Art. no. 3Mar., doi:10.1038/nmat3568.
- [33] D.G. Cahill, Analysis of heat flow in layered structures for time-domain thermoreflectance, *Rev. Sci. Instrum.* 75 (12) (2004) 5119–5122 Dec., doi:10.1063/1.1819431.
- [34] J. Yang, C. Maragliano, A.J. Schmidt, Thermal property microscopy with frequency domain thermoreflectance, *Rev. Sci. Instrum.* 84 (10) (2013) 104904 Oct., doi:10.1063/1.4824143.
- [35] A.J. Schmidt, R. Cheaito, M. Chiesa, A frequency-domain thermoreflectance method for the characterization of thermal properties, *Rev. Sci. Instrum.* 80 (9) (2009) 094901 Sep., doi:10.1063/1.3212673.
- [36] A.J. Schmidt, R. Cheaito, M. Chiesa, Characterization of thin metal films via frequency-domain thermoreflectance, *J. Appl. Phys.* 107 (2) (2010) 024908 Jan., doi:10.1063/1.3289907.
- [37] S. Cho, K.H. Lim, S.Y. Park, Z. Yin, J. Yoo, Y.S. Kim, Pressure-assisted electrode fabrication using simply synthesized  $\text{Cu}_3\text{Sn}$  Sn alloy nanoparticles, *J. Mater. Chem. C* 3 (12) (2015) 2773–2777, doi:10.1039/C5TC00215J.
- [38] H.P.R. Frederikse, R.J. Fields, A. Feldman, Thermal and electrical properties of copper-tin and nickel-tin intermetallics, *J. Appl. Phys.* 72 (7) (1992) 2879–2882 Oct., doi:10.1063/1.351487.

- [39] D.C. Langreth, M.J. Mehl, Beyond the local-density approximation in calculations of ground-state electronic properties, *Phys. Rev. B* 28 (4) (1983) 1809–1834 Aug., doi:10.1103/PhysRevB.28.1809.
- [40] J.P. Perdew, K. Burke, M. Ernzerhof, Generalized gradient approximation made simple, *Phys. Rev. Lett.* 77 (18) (1996) 3865–3868 Oct., doi:10.1103/PhysRevLett.77.3865.
- [41] G. Kresse, J. Hafner, Ab initio molecular dynamics for liquid metals, *Phys. Rev. B* 47 (1) (1993) 558–561 Jan., doi:10.1103/PhysRevB.47.558.
- [42] G. Kresse, J. Furthmüller, Efficient iterative schemes for ab initio total-energy calculations using a plane-wave basis set, *Phys. Rev. B* 54 (16) (1996) 11169–11186 Oct., doi:10.1103/PhysRevB.54.11169.
- [43] P.E. Blöchl, Projector augmented-wave method, *Phys. Rev. B* 50 (24) (1994) 17953–17979 Dec., doi:10.1103/PhysRevB.50.17953.
- [44] J.P. Perdew, A. Zunger, Self-interaction correction to density-functional approximations for many-electron systems, *Phys. Rev. B* 23 (10) (1981) 5048–5079 May, doi:10.1103/PhysRevB.23.5048.
- [45] A. Togo, I. Tanaka, First principles phonon calculations in materials science, *Scr. Mater.* 108 (2015) 1–5 Nov., doi:10.1016/j.scriptamat.2015.07.021.
- [46] A.A. Mostofi, et al., An updated version of wannier90: a tool for obtaining maximally-localised Wannier functions, *Comput. Phys. Commun.* 185 (8) (2014) 2309–2310 Aug., doi:10.1016/j.cpc.2014.05.003.
- [47] G. Pizzi, D. Volja, B. Kozinsky, M. Fornari, N. Marzari, BoltzWann: a code for the evaluation of thermoelectric and electronic transport properties with a maximally-localized Wannier functions basis, *Comput. Phys. Commun.* 185 (1) (2014) 422–429 Jan., doi:10.1016/j.cpc.2013.09.015.
- [48] J. Noffsinger, F. Giustino, B.D. Malone, C.H. Park, S.G. Louie, M.L. Cohen, EPW: a program for calculating the electron-phonon coupling using maximally localized Wannier functions, *Comput. Phys. Commun.* 181 (12) (2010) 2140–2148 Dec., doi:10.1016/j.cpc.2010.08.027.
- [49] S. Poncé, E.R. Margine, F. Giustino, Towards predictive many-body calculations of phonon-limited carrier mobilities in semiconductors, *Phys. Rev. B* 97 (12) (2018) 121201 Mar., doi:10.1103/PhysRevB.97.121201.
- [50] P. Giannozzi, et al., Advanced capabilities for materials modelling with quantum ESPRESSO, *J. Phys. Condens. Matter* 29 (46) (2017) 465901 Oct., doi:10.1088/1361-648X/aa8f79.
- [51] A. Togo, L. Chaput, I. Tanaka, Distributions of phonon lifetimes in Brillouin zones, *Phys. Rev. B* 91 (9) (2015) 094306 Mar., doi:10.1103/PhysRevB.91.094306.
- [52] S. Hajinazar, A. Thorn, E.D. Sandoval, S. Kharabazde, A.N. Kolmogorov, MAISE: construction of neural network interatomic models and evolutionary structure optimization, *Comput. Phys. Commun.* 259 (2021) 107679 Feb., doi:10.1016/j.cpc.2020.107679.
- [53] S. Hajinazar, J. Shao, A.N. Kolmogorov, Stratified construction of neural network based interatomic models for multicomponent materials, *Phys. Rev. B* 95 (1) (2017) 014114 Jan., doi:10.1103/PhysRevB.95.014114.
- [54] M.D. Vaudin, Pseudosymmetry in EBSD patterns, *Microsc. Microanal.* 11 (S02) (2005), doi:10.1017/S143192760500710.
- [55] “Ellipsoid fit.” <https://www.mathworks.com/matlabcentral/fileexchange/24693-ellipsoid-fit> (accessed May 20, 2020).
- [56] T. Yamane, N. Nagai, S. Katayama, M. Todoki, Measurement of thermal conductivity of silicon dioxide thin films using a  $3\omega$  method, *J. Appl. Phys.* 91 (12) (2002) 9772, doi:10.1063/1.1481958.
- [57] S.M. Lee, D.G. Cahill, Heat transport in thin dielectric films, *J. Appl. Phys.* 81 (6) (1997) 2590–2595 Mar., doi:10.1063/1.363923.
- [58] H.C. Chien, D.J. Yao, M.J. Huang, T.Y. Chang, Thermal conductivity measurement and interface thermal resistance estimation using SiO<sub>2</sub> thin film, *Rev. Sci. Instrum.* 79 (5) (2008) 054902 May, doi:10.1063/1.2927253.
- [59] Y. Terada, K. Ohkubo, T. Mohri, T. Suzuki, Thermal conductivity of intermetallic compounds with metallic bonding, *Mater. Trans.* 43 (12) (2002) 3167–3176, doi:10.2320/matertrans.43.3167.
- [60] E. Goldratt, A.J. Greenfield, Experimental test of the Wiedemann-Franz law for indium, *J. Phys. F Met. Phys.* 10 (3) (1980) L95–L99 Mar., doi:10.1088/0305-4608/10/3/001.
- [61] Y. Terada, K. Ohkubo, T. Mohri, T. Suzuki, Thermal conductivity of intermetallic compounds with metallic bonding, *Mater. Trans.* 43 (12) (2002) 3167–3176, doi:10.2320/matertrans.43.3167.
- [62] Y. Terada, K. Ohkubo, T. Mohri, T. Suzuki, Site preference in NiAl-determination by thermal conductivity measurement, *Mater. Sci. Eng. A* 329–331 (2002) 468–473 Jun., doi:10.1016/S0921-5093(01)01622-7.
- [63] A. Giri, M.V. Tokina, O.V. Prezhdo, P.E. Hopkins, Electron-phonon coupling and related transport properties of metals and intermetallic alloys from first principles, *Mater. Today Phys.* (2020) 100175 Jan., doi:10.1016/j.mtphys.2019.100175.
- [64] C.T. Heycock, F.H. Neville, Bakerian lecture-on the constitution of the copper-tin series of alloys, *Proc. R. Soc. Lond.* 71 (467–476) (1903) 409–412 Jun., doi:10.1098/rspl.1902.0117.
- [65] S. Fürtauer, D. Li, D. Cupid, H. Flandorfer, The Cu–Sn phase diagram, part I: new experimental results, *Intermetallics* 34 (2013) 142–147 Mar., doi:10.1016/j.intermet.2012.10.004.
- [66] X. Sang, K. Du, H. Ye, An ordered structure of Cu<sub>3</sub>Sn in Cu–Sn alloy investigated by transmission electron microscopy, *J. Alloy. Compd.* 469 (1–2) (2009) 129–136 Feb., doi:10.1016/j.jallcom.2008.01.107.
- [67] E.C. Bain, Cored crystals and metallic compounds, *Chem. Metall. Eng.* 23 (1923) 65–69.
- [68] D. Qu, C. Li, L. Bao, Z. Kong, Y. Duan, Structural, electronic, and elastic properties of orthorhombic, hexagonal, and cubic Cu<sub>3</sub>Sn intermetallic compounds in Sn–Cu lead-free solder, *J. Phys. Chem. Solids* 138 (2020) 109253 Mar., doi:10.1016/j.jpcs.2019.109253.
- [69] R. Grau-Crespo and S. Hamad, The symmetry-adapted configurational ensemble approach to the computer simulation of site-disordered solids, MOL2NET15, Conference on Molecular, Biomedical & Computational Sciences and Engineering, 2015, pp. 1–21 Dec., doi:10.3390/MOL2NET-1-c002.
- [70] U. Becker, A. Fernández-González, M. Prieto, R. Harrison, A. Putnis, Direct calculation of thermodynamic properties of the barite/celestite solid solution from molecular principles, *Phys. Chem. Miner.* 27 (4) (2000) 291–300 Mar., doi:10.1007/s002690050258.
- [71] Y. Koizumi, H. Katsumura, Y. Minamino, N. Tsuji, J.G. Lee, H. Mori, Growth kinetics of antiphase domain in Ti<sub>3</sub>Al intermetallic compound, *Sci. Technol. Adv. Mater.* 5 (1–2) (2004) 19–28 Jan., doi:10.1016/j.stam.2003.10.016.
- [72] Y. Koizumi, T. Fujita, Y. Minamino, Anomalous growth of antiphase domains in Ti<sub>3</sub>Al, *Scr. Mater.* 60 (3) (2009) 144–147 Feb., doi:10.1016/j.scriptamat.2008.09.017.
- [73] A.G. Van Der Geest, A.N. Kolmogorov, Stability of 41 metal-boron systems at 0GPa and 30GPa from first principles, *Calphad Comput. Coupling Phase Diagr. Thermochem.* 46 (2014) 184–204 Sep., doi:10.1016/j.calphad.2014.03.005.
- [74] S. Curtarolo, D. Morgan, G. Ceder, Accuracy of ab initio methods in predicting the crystal structures of metals: a review of 80 binary alloys, *Comput. Coupling Phase Diagr. Thermochem.* 29 (2005) 163–211, doi:10.1016/j.calphad.2005.01.002.
- [75] Y. Zhang, G. Kresse, C. Wolverton, Nonlocal first-principles calculations in Cu–Au and other intermetallic alloys, *Phys. Rev. Lett.* 112 (7) (2014) 075502 Feb., doi:10.1103/PhysRevLett.112.075502.
- [76] G. Ghosh, Phase stability and cohesive properties of Au–Sn intermetallics: a first-principles study, *J. Mater. Res.* 23 (5) (2008) 1398–1416 May, doi:10.1557/JMR.2008.0175.
- [77] A.F. Bialon, T. Hammerschmidt, R. Drautz, S. Shah, E.R. Margine, A.N. Kolmogorov, Possible routes for synthesis of new boron-rich Fe–B and Fe1–xCrxB<sub>4</sub> compounds, *Appl. Phys. Lett.* 98 (8) (2011) 081901 Feb., doi:10.1063/1.3556564.
- [78] H. Niu, et al., Structure, bonding, and possible superhardness of CrB<sub>4</sub>, *Phys. Rev. B Condens. Matter Mater. Phys.* 85 (14) (2012) 144116 Apr., doi:10.1103/PhysRevB.85.144116.
- [79] S.K. Choi, et al., Spin waves and revised crystal structure of honeycomb iridate Na<sub>2</sub>IrO<sub>3</sub>, *Phys. Rev. Lett.* 108 (12) (2012) 127204 Mar., doi:10.1103/PhysRevLett.108.127204.
- [80] A.N. Kolmogorov, S. Curtarolo, Prediction of different crystal structure phases in metal borides: a lithium monoboride analog to Mg B<sub>2</sub>, *Phys. Rev. B Condens. Matter Mater. Phys.* 73 (18) (2006) 180501 May, doi:10.1103/PhysRevB.73.180501.
- [81] A.N. Kolmogorov, S. Hajinazar, C. Angyal, V.L. Kuznetsov, A.P. Jephcoat, Synthesis of a predicted layered LiB via cold compression, *Phys. Rev. B Condens. Matter Mater. Phys.* 92 (14) (2015) 144110 Oct., doi:10.1103/PhysRevB.92.144110.
- [82] A.N. Kolmogorov, S. Shah, E.R. Margine, A.K. Kleppe, A.P. Jephcoat, Pressure-driven evolution of the covalent network in CaB<sub>6</sub>, *Phys. Rev. Lett.* 109 (7) (2012) 075501 Aug., doi:10.1103/PhysRevLett.109.075501.
- [83] A.N. Kolmogorov, S. Shah, E.R. Margine, A.F. Bialon, T. Hammerschmidt, R. Drautz, New superconducting and semiconducting Fe–B compounds predicted with an Ab initio evolutionary search, *Phys. Rev. Lett.* 105 (21) (2010) 217003 Nov., doi:10.1103/PhysRevLett.105.217003.
- [84] H. Gou, et al., Discovery of a superhard iron tetraboride superconductor, *Phys. Rev. Lett.* 111 (15) (2013) 157002 Oct., doi:10.1103/PhysRevLett.111.157002.
- [85] J. Shao, C. Beaufils, A.N. Kolmogorov, Ab initio engineering of materials with stacked hexagonal tin frameworks, *Sci. Rep.* 6 (1) (2016) 28369 Sep., doi:10.1038/srep28369.
- [86] A.N. Kolmogorov, S. Curtarolo, Theoretical study of metal borides stability, *Phys. Rev. B Condens. Matter Mater. Phys.* 74 (22) (2006) 224507 Dec., doi:10.1103/PhysRevB.74.224507.
- [87] Z. Tong, S. Li, X. Ruan, H. Bao, Comprehensive first-principles analysis of phonon thermal conductivity and electron-phonon coupling in different metals, *Phys. Rev. B* 100 (14) (2019) 144306 Oct., doi:10.1103/PhysRevB.100.144306.
- [88] Y. Wang, Z. Lu, X. Ruan, First principles calculation of lattice thermal conductivity of metals considering phonon-phonon and phonon-electron scattering, *J. Appl. Phys.* 119 (22) (2016) 225109 Jun., doi:10.1063/1.4953366.
- [89] J.M. Ziman, *Electrons and Phonons: The Theory of Transport Phenomena in Solids*, Oxford University Press, Oxford, 2001, doi:10.1093/acprof:oso/9780198507796.001.0001.
- [90] N.E. Lee, J.J. Zhou, L.A. Agapito, M. Bernardi, Charge transport in organic molecular semiconductors from first principles: the bandlike hole mobility in a naphthalene crystal, *Phys. Rev. B* 97 (11) (2018) 115203 Mar., doi:10.1103/PhysRevB.97.115203.
- [91] Y.P. Mizuta, F. Ishii, Large anomalous Nernst effect in a skyrmion crystal, *Sci. Rep.* 6 (1) (2016) Art. no. 1, Jun., doi:10.1038/srep28076.
- [92] R.L. González-Romero, C.R. Miranda, M.A. Avila, A. Antonelli, Hosting of La<sup>3+</sup> guest ions in type-I Ge clathrates: a first-principles characterization for thermoelectric applications, *Comput. Mater. Sci.* 122 (2016) 46–56 Sep., doi:10.1016/j.commatsci.2016.05.013.
- [93] I.O.A. Ali, D.P. Joubert, M.S.H. Suleiman, A theoretical investigation of structural, mechanical, electronic and thermoelectric properties of orthorhombic CH<sub>3</sub>NH<sub>3</sub>Pb<sub>3</sub>, *Eur. Phys. J. B* 91 (10) (2018) 263 Oct., doi:10.1140/epj/b/e2018-90312-5.

- [94] R.L. González-Romero, A. Antonelli, Estimating carrier relaxation times in the  $\text{Ba}_8\text{Ga}_{16}\text{Ge}_{30}$  clathrate in the extrinsic regime, *Phys. Chem. Chem. Phys.* 19 (4) (2017) 3010–3018 Jan., doi:[10.1039/C6CP08026J](https://doi.org/10.1039/C6CP08026J).
- [95] K. Chen, B. Du, N. Bonini, C. Weber, H. Yan, M.J. Reece, Theory-guided synthesis of an eco-friendly and low-cost copper based sulfide thermoelectric material, *J. Phys. Chem. C* 120 (48) (2016) 27135–27140 Dec., doi:[10.1021/acs.jpcc.6b09379](https://doi.org/10.1021/acs.jpcc.6b09379).
- [96] S. Poncé, F. Giustino, Structural, electronic, elastic, power, and transport properties of  $\beta\text{-Ga}_2\text{O}_3$  from first principles, *Phys. Rev. Res.* 2 (3) (2020) 033102 Jul., doi:[10.1103/PhysRevResearch.2.033102](https://doi.org/10.1103/PhysRevResearch.2.033102).
- [97] Y. Su, K.K. Song, M. Zhong, L.B. Shi, P. Qian, Stability and phonon-limited mobility for  $\text{CsSnI}_3$  and  $\text{CsPbI}_3$ , *J. Alloy. Compd.* 889 (2021) 161723 Dec., doi:[10.1016/j.jallcom.2021.161723](https://doi.org/10.1016/j.jallcom.2021.161723).
- [98] K.C. Zhang, L.Y. Cheng, C. Shen, Y.F. Li, Y. Liu, Y. Zhu, Thickness-dependent anisotropic transport of phonons and charges in few-layered  $\text{PdSe}_2$ , *Phys. Chem. Chem. Phys.* 23 (34) (2021) 18869–18884 Sep., doi:[10.1039/D1CP00992C](https://doi.org/10.1039/D1CP00992C).
- [99] W. Setyawan, S. Curtarolo, High-throughput electronic band structure calculations: challenges and tools, *Comput. Mater. Sci.* 49 (2) (2010) 299–312 Aug., doi:[10.1016/j.commatsci.2010.05.010](https://doi.org/10.1016/j.commatsci.2010.05.010).
- [100] L. Li, A. Slocombe, K.L. Ng, Selective laser sintering of compacted Cu/Sn powders, *Int. Congr. Appl. Lasers Electro Opt.* 1998 (1) (1998) E38–E47 Nov., doi:[10.2351/1.5059150](https://doi.org/10.2351/1.5059150).
- [101] J. Towns, et al., XSEDE: accelerating scientific discovery, *Comput. Sci. Eng.* 16 (5) (2014) 62–74 Sep., doi:[10.1109/MCSE.2014.80](https://doi.org/10.1109/MCSE.2014.80).